Journal of Alloys and Compounds 1045 (2025) 184716

Contents lists available at ScienceDirect

Journal of Alloys and Compounds

journal homepage: www.elsevier.com/locate/jalcom

Cold sintering of silicon nitride using surface-amorphous silica

Yeongjun Seo [a,*], Masaya Minehira [a], Sunghun Cho [a], Tomoyo Goto [a,b], Yoshifumi Kondo [a], Do Hyung Han [a], Tohru Sekino [a,*]

[a] SANKEN, The University of Osaka, 8-1 Mihogaoka, Ibaraki, Osaka 567-0047, Japan
[b] Graduate School of Science and Technology, Nara Institute of Science and Technology (NAIST), 8916-5 Takayama-cho, Ikoma, Nara 630-0192, Japan

ARTICLE INFO

Keywords:
Cold sintering process
Mechanochemical reaction
Silicon nitride
Silica
Low-temperature sintering

ABSTRACT

This study demonstrated the densification of silicon nitride (Si_3N_4) via cold sintering using amorphous silica (SiO_2) as the bonding phase. Amorphous SiO_2 was incorporated onto the surfaces of Si_3N_4 particles using a mechanochemical reaction via planetary ball milling with ultrapure water at room temperature. Increasing the SiO_2 content on the Si_3N_4 particle surfaces improved the relative density of the cold-sintered Si_3N_4 samples, achieving a maximum value of 78.4 % at 160 °C and 500 MPa. Additionally, the addition of 5 wt% SiO_2 nanoparticles to the Si_3N_4 powders before milling further increased the surface SiO_2 content, which enhanced the dissolution–reprecipitation of SiO_2 at the Si_3N_4 interfaces and increased the relative density to 86.2 %. The cold-sintered Si_3N_4 samples exhibited improved mechanical properties with longer milling durations, achieving a Vickers hardness of 2.53 ± 0.09 GPa, biaxial flexural strength of 169.4 ± 12.3 MPa, and Young's modulus of 113.1 ± 1.5 GPa. This approach enables the low-temperature densification of ceramic materials that are otherwise difficult to dissolve by incorporating soluble phases. This energy-efficient method holds promise for the development of novel ceramic processes with a low environmental impact.

1. Introduction

Silicon nitride (Si_3N_4) ceramics are widely used as structural materials because of their excellent mechanical properties, which include a high toughness, thermal shock resistance, high strength, wear resistance, high-temperature mechanical strength, corrosion resistance, and electrical insulation [1–3]. They have two types of crystal structures: a low-temperature stable α-phase (trigonal) and high-temperature stable β-phase (hexagonal) [4]. During the liquid-phase-sintering process, a phase transition from the α-phase to the β-phase occurs in a temperature range of approximately 1400–1600 °C [1,5], accompanied by particle dissolution and reprecipitation. This transition leads to the growth of elongated β-phase rod-like crystals, which form a complex network of interlocking grains, thereby resulting in excellent mechanical and thermal properties [1–3]. Owing to these properties, Si_3N_4 ceramics are widely used in engineering applications such as gas turbines, bearings, and automotive engine components [6–8].

Despite their excellent properties, Si_3N_4 ceramics encounter significant sintering challenges because of the high sintering temperatures required. Unlike oxide-based ceramics with ionic bonding, α-Si_3N_4 has strong covalent Si-N bonds, resulting in a low diffusion coefficient at high temperatures [9]. In addition, the surface silica (SiO_2) impurities in Si_3N_4 ceramics volatilize as SiO (g) at high temperatures, repeatedly evaporating and condensing, thereby hampering densification [10]. This hinders the atomic diffusion, which increases the sintering temperature of Si_3N_4. To overcome these problems, liquid-phase-assisted hot-press [11] and gas-pressure [12,13] sintering have been used with various sintering aids such as Y_2O_3, Al_2O_3, and MgO [11–15]. However, the sintering temperature of Si_3N_4 ceramics is at least 1500 °C, resulting in a significant environmental impact and energy consumption. Therefore, it is essential to develop new sintering processes that fundamentally reduce the sintering temperature.

The cold sintering process (CSP) has recently emerged as a sintering technique for densifying inorganic particles at remarkably low temperatures (below 300 °C) [16–18]. The primary driving force behind the CSP is the transient liquid phase, which facilitates a unique densification mechanism. In the CSP, the base particles are mixed with a solvent and then compressed and heated, which differs significantly from traditional high-temperature techniques. This process promotes particle rearrangement and enhanced particle-to-particle contact. Simultaneously, the solvent partially dissolves the surface atoms or ions of the inorganic particles at their contact points. These dissolved species then migrate

* Corresponding authors.
E-mail addresses: yjseo@sanken.osaka-u.ac.jp (Y. Seo), sekino@sanken.osaka-u.ac.jp (T. Sekino).

https://doi.org/10.1016/j.jallcom.2025.184716
Received 5 September 2025; Received in revised form 27 October 2025; Accepted 27 October 2025
Available online 28 October 2025

through the liquid phase owing to the chemical potential gradient and reprecipitate on the surfaces of other particles. This dissolution–reprecipitation process is crucial for the CSP because it promotes solid-state bonding between particles. Consequently, the voids and pores are filled, leading to the effective densification of the material. However, the CSP has the limitation that it is difficult to densify ceramic materials that are hardly soluble in solvents or hydrothermal environments [16]. For these materials, a bonding phase that dissolves relatively easily in solvents has been used to enable CSP densification. Yamaguchi et al. [19] fabricated SiC/SiO_2 ceramics with a relative density of 80 % via the CSP at 200 °C using SiC particles with amorphous SiO_2 layers formed via heat treatment at 1100 °C. Similarly, Induja and Sebastian [20] fabricated Al_2O_3/NaCl composites with a relative density of 96 % via the CSP at 120 °C based on the dissolution–reprecipitation of NaCl. With regard to Si_3N_4, previous research has explored the fabrication of cold-sintered Si_3N_4@SiO_2/PEEK core–shell composites in which the SiO_2 bonding phase was prepared via the Stöber method using tetraethyl orthosilicate[21,22]. These studies highlighted the critical role of the bonding phase in enabling the cold sintering of ceramic materials that are otherwise difficult to densify solely via the dissolution–reprecipitation of the base material.

Mechanochemical grinding methods have been widely used as effective approaches for producing amorphous layers on the surfaces or interfaces of diverse materials [23–25]. In particular, the high-energy ball milling of silicon-containing precursors, such as Si_3N_4 or silicon powder, can induce the formation of amorphous SiO_2. In the presence of an oxidizing agent (e.g., O_2, H_2O, or air), surface oxidation and tribochemical reactions lead to the in-situ formation of an amorphous SiO_2 layer [25–27]. This surface oxide not only modifies the interparticle bonding characteristics but also serves as a reactive phase in subsequent processes, such as the CSP. Accordingly, the mechanochemical formation of SiO_2 provides a scalable strategy for tailoring the surface chemistry and enabling low-temperature densification while avoiding conventional thermal oxidation and complex wet-chemical synthesis routes such as the Stöber method.

In this study, a mechanochemical reaction was employed to form a SiO_2 layer on the surfaces of Si_3N_4 particles by planetary ball milling in ultrapure water, offering a simple and effective strategy for achieving the low-temperature densification of Si_3N_4 via the CSP. Unlike conventional high-temperature sintering, where the native SiO_2 on Si_3N_4 surfaces tends to decompose and hinder densification [10], in this case, the native oxide plays a favorable role in the mechanochemical process by promoting the further growth of the SiO_2 layer. In addition to the SiO_2 layer formation, the milling process can reduce the Si_3N_4 particle size, which enhances the densification by increasing the surface energy. To further improve the densification by increasing the amount of the bonding phase, SiO_2 nanoparticles were introduced prior to planetary ball milling, complementing the surface oxide layer formed via mechanochemical reactions. To this end, various milling times were employed as key parameters to control the Si_3N_4 particle size and thickness of the SiO_2 surface layer. An NaOH solution was selected for use with the CSP because of its ability to effectively dissolve the amorphous SiO_2 phase, facilitating the dissolution–reprecipitation mechanism. The correlation between SiO_2 formation via mechanochemical reactions and the densification behavior was thoroughly investigated. Furthermore, the microstructural, structural, and mechanical properties of the cold-sintered samples were comprehensively determined.

2. Material and methods

2.1. Formation of SiO_2 on the surfaces of the Si_3N_4 particles

Commercially available α-Si_3N_4 powder (SN-E10, Ube corporation, Tokyo, Japan) was ball-milled in a planetary ball mill (Pulverisette-7, Fritsch GmbH, Idar-Oberstein, Germany) using ultrapure water as the liquid medium to promote SiO_2 formation. Milling was performed in a tungsten carbide (WC) jar using WC balls at a ball-to-powder ratio of 10:1, with the mill operated at 300 rpm for different durations (1, 3, 5, and 10 h). After planetary ball milling, the powders were separated from the ultrapure water using an evaporator and dried overnight in an oven. The pure Si_3N_4 powder was referred to as pure SN, and the Si_3N_4 powder samples milled for 1, 3, 5, and 10 h were denoted as SN_BM1h, SN_BM3h, SN_BM5h, and SN_BM10h, respectively. To further increase the amount of SiO_2 on the surfaces of the Si_3N_4 particles, 5 wt% amorphous SiO_2 nanoparticles (Sigma-Aldrich, Saint Louis, USA) were added to Si_3N_4 powder samples, which were then ball-milled under the same conditions for 1, 3, 5, and 10 h, and labeled as SN/5SiO_2_BM1h, SN/5SiO_2_BM3h, SN/5SiO_2_BM5h, and SN/5SiO_2_BM10h, respectively.

2.2. Cold sintering of the pure and ball-milled Si_3N_4 powders

For densification using the CSP, each powder sample (pure SN, SN_BM, and SN/5SiO_2_BM) was thoroughly mixed with a 10 wt%, 10 mol/L NaOH solution using a mortar and pestle. Subsequently, each mixture was placed in a mold with a diameter of 12 mm and heated at 160 °C under a uniaxial pressure of 500 MPa for 1 h using a ring heater (Sansho Industry Co., Ltd., Osaka, Japan) and uniaxial press (Newton Press, NT-100H, NPa System Co., Ltd., Saitama, Japan). For comparison, SN_BM10h was mixed with 5 wt% SiO_2 nanoparticles using a mortar and pestle, and subsequently densified using the same CSP conditions. After cooling the mold to room temperature, the applied pressure was slowly released to avoid crack generation, and the densified pellets were carefully removed from the mold. Subsequently, all of the cold-sintered samples were dried in an oven to remove excess moisture.

2.3. Characterization

The pure SN, SN_BM, and SN/5SiO_2_BM powders were observed using field-emission scanning electron microscopy (FE-SEM; SU9000, Hitachi High-Tech Corp., Tokyo, Japan) equipped with an energy-dispersive X-ray (EDX) detector at an accelerating voltage of 30 kV. The SiO_2 formation in each powder sample was examined using X-ray diffraction (XRD; D8 Advance, Bruker AXS GmbH, Karlsruhe, Germany) with a Cu Kα radiation source ($\lambda = 1.54178$ Å) at 40 kV and 40 mA, along with Fourier-transform infrared spectroscopy (FT-IR; FT/IR-6600, JASCO Corp., Tokyo, Japan). X-ray photoelectron spectroscopy (XPS; JPS9010MX, JEOL Ltd., Tokyo, Japan) was used to determine the thickness [d_{XPS} (nm)] of SiO_2 on the surfaces of each powder sample. Based on the XPS results, the d_{XPS} value was calculated from the Si 2p oxide-to-nitride peak ratio using Eq. (1)[28]:

$$d_{XPS} = \lambda \ln\left(\frac{I_O}{I_N}\frac{I_N^0}{I_O^0} + 1\right) \quad (1)$$

where λ is the mean escape depth of electrons during photoemission; I_O and I_N denote the measured intensities for O 1 s and N 1 s, respectively; and I_O^0 and I_N^0 are the theoretical intensities for pure Si_3N_4 and SiO_2, respectively. The $\frac{I_N^0}{I_O^0}$ ratio reported by Peuckert and Geril is 1.03 [28], and the value of λ was set to 1.99 nm. Transmission electron microscopy (TEM; JEM-ARM200F, JEOL Ltd., Tokyo, Japan) equipped with EDX detector was used to observe the surface SiO_2 phase on the Si_3N_4 particles. In addition, the average particle sizes of pure SN and SN_BM were determined using dynamic light scattering (Zetasizer Nano ZS, Malvern Instruments Ltd., Malvern, UK). The bulk densities of the cold-sintered samples were determined using the Archimedes method with absolute ethanol (EtOH, 99.5 %, FUJIFILM Wako Pure Chemical Corp., Osaka, Japan) as the liquid medium. The true densities were measured using a helium gas pycnometer (Accupyc II 1340, Micromeritics Inc., GA, USA) and used to calculate the relative densities. The fracture surfaces of the cold-sintered samples were observed using FE-SEM. The mechanical properties of the cold-sintered SN/5SiO_2 samples were evaluated. A

Vickers hardness tester (FV-310e; Future-Tech Corp., Kanagawa, Japan) was used to measure the Vickers hardness of each of the cold-sintered samples by applying a load of 9.8 N for 15 s. The biaxial flexural strengths of the cold-sintered samples were evaluated using the piston-on-three-ball method. The measurements were conducted using a universal testing machine (AGX-10kNVD, Shimadzu Corp., Kyoto, Japan) equipped with a 5 kN load cell operating at a crosshead speed of 0.5 mm/min. Cold-sintered samples with a diameter of 12 mm were supported by three equidistant balls arranged at 120° intervals along a supporting circle, whereas a piston applied a load centrally on the opposite surface. The Young's modulus was determined using the ultrasonic pulse-echo technique, which involves measuring the ultrasonic velocity using a digital storage oscilloscope (DSOX3052T, Keysight, Tokyo, Japan) and an ultrasonic pulser/receiver (Model 5072, PANAMETRICS, MA, USA). Each sample was subjected to six measurements for each property, and the mean values were recorded.

3. Results and discussion

3.1. Formation of SiO_2 on Si_3N_4 particles via planetary ball milling

After planetary ball-milling the Si_3N_4 powder samples with ultrapure water for different durations, the obtained powders were observed using FE-SEM (Fig. 1). Compared to the pure SN powder (Fig. 1(a)), the SN_BM powders exhibited smaller particle sizes as the milling time increased (Fig. 1(b)–(e)). Specifically, as shown in Fig. 1(f), the average particle size of the pure SN was determined to be 677.6 ± 62.3 nm, which drastically decreased to 375.6 ± 37.9 nm after milling for 3 h (SN_BM3h). The size further decreased to 277.6 ± 38.9 nm after 10 h of milling (SN_BM10h), or less than half of its original value. However, longer milling times may cause contamination of the powder owing to the wear of the milling balls and jar. To verify this, SEM-EDX mapping analysis was performed on the powders as a function of the milling time (Fig. S1). As a result, tungsten (W) was detected in addition to the original constituents, which was attributed to the wear of the milling media (WC). The elemental composition results based on the SEM-EDX analysis revealed that the W content increased with the milling time, reaching 1.9, 2.3, 3.0, and 4.8 mass% after 1, 3, 5, and 10 h of milling, respectively.

XRD and FT-IR analyses were conducted to detect the SiO_2 formation (Fig. 2). As shown in Fig. 2(a), all of the samples only exhibited peaks corresponding to crystalline α-Si_3N_4 (PDF no. 00–041–0360), with no peaks related to W or its compounds detected. However, for the SN_BM powders, broad hump patterns were observed in the 2θ range of 10—60° (Fig. 2(b)) with increasing milling time, which is a characteristic of amorphous SiO_2[29,30]. In addition, as shown in Fig. 2(c) and (d), with an increase in the milling time, peaks corresponding to the −OH groups owing to the use of ultrapure water as the milling medium were observed at 3368 and 1638 cm^{-1}, while a peak corresponding to the Si-O bond appeared at 1095 cm^{-1}, suggesting the increased formation of SiO_2 in the SN_BM powders [21,31]. This oxidation was attributed to the mechanochemical reaction of Si_3N_4 with H_2O. During the planetary ball milling, the friction and wear of the Si_3N_4 particles initially resulted in a high wear rate, but the water eventually produced a strong lubrication effect, thereby forming a SiO_2 layer. The possible chemical reaction is shown in Eq. (2)[26,27].

$$Si_3N_4 + 6H_2O \rightarrow 3SiO_2 + 4NH_3\uparrow \quad (2)$$

XPS and TEM analyses were conducted to further investigate the SiO_2 content on the surfaces of the Si_3N_4 particles (Figs. 3 and 4, respectively). As shown in Fig. 3(a)–(e), the XPS Si 2p spectra of the pure SN and SN_BM powders were deconvoluted into three peaks at 101.7, 103.1, and 103.7 eV, corresponding to the Si-N, O-Si-N, and Si-O groups, respectively [32–34]. Increases in both the Si-O and O-Si-N peak areas, which were associated with the SiO_2 formation, were observed with increasing milling time.

To enable a quantitative comparison, the area ratios of Si-O (%) and d_{XPS} (nm) were calculated from the devolution spectra and intensities of the O 1 s and N 1 s peaks in the wide-scan XPS profiles (Fig. 3(f)) and plotted against the milling time (Fig. 3(g)). The pure SN powder particles had a native SiO_2 phase on their surfaces, with the Si-O peak ratio and d_{XPS} determined to be 6.6 % and 1.1 nm, respectively. However, after planetary ball milling, both values increased with the milling time, suggesting that the reaction shown in Eq. (2) proceeded progressively. SN_BM10h exhibited the highest values, with a Si-O peak ratio of 11.4 % and d_{XPS} value of 1.6 nm.

Because the d_{XPS} values were calculated under the assumption that SiO_2 was formed as a layer on the surfaces of the Si_3N_4 particles, the

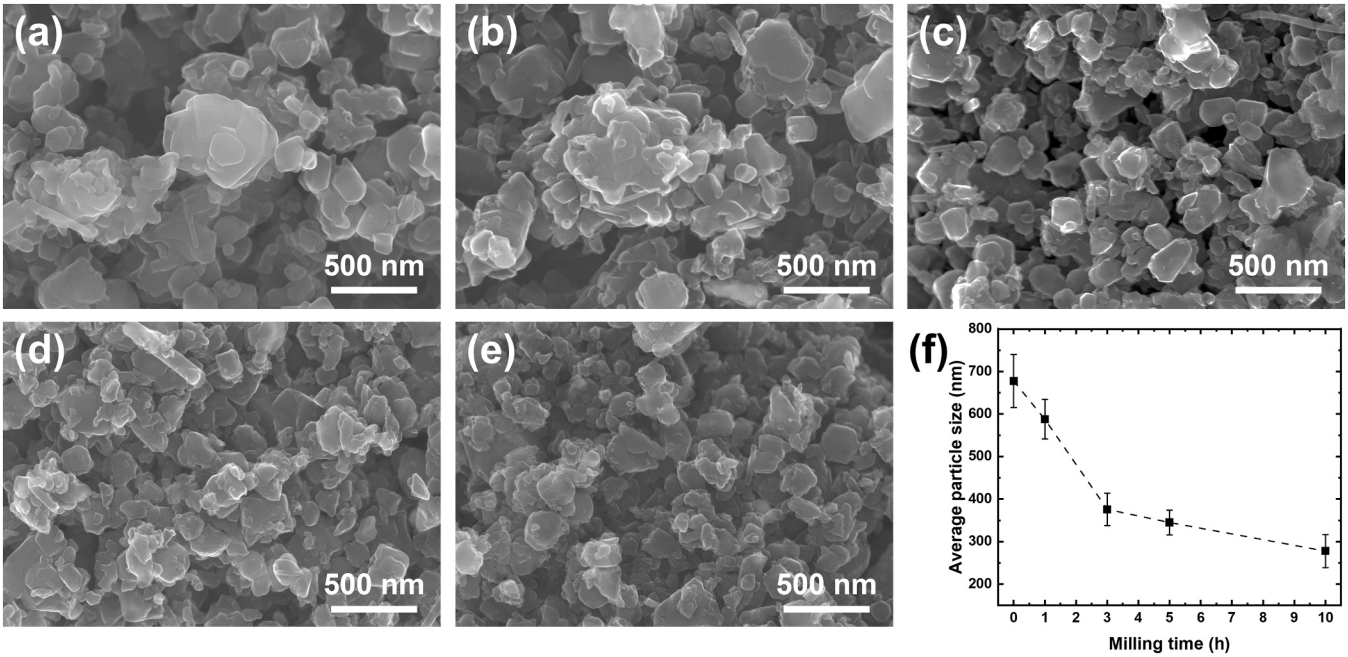

Fig. 1. SEM images of (a) pure SN, (b) SN_BM1h, (c) SN_BM3h, (d) SN_BM5h, and (e) SN_BM10h. (f) Average particle sizes of pure SN and SN_BM powders.

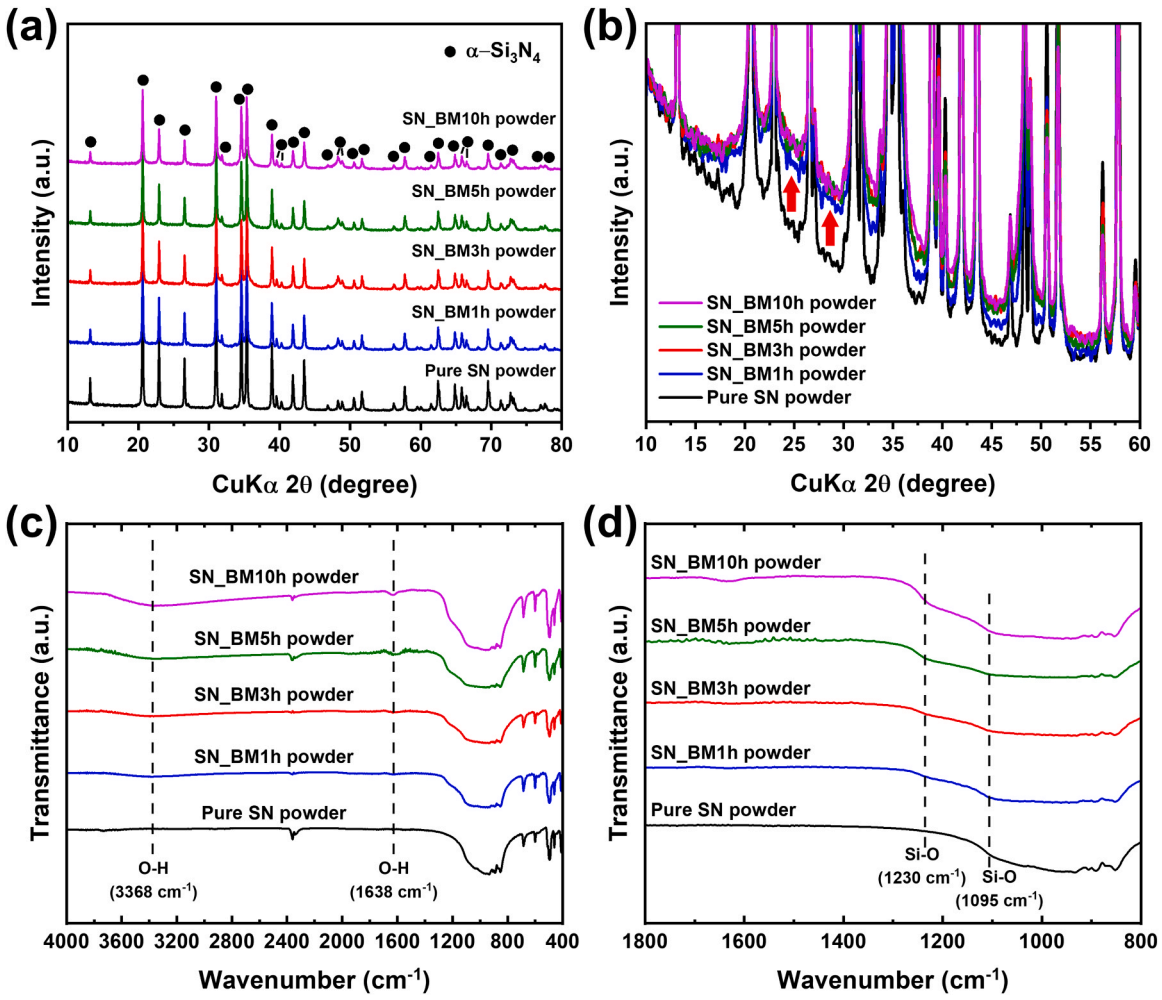

Fig. 2. (a) XRD patterns in the range of 2θ = 10–80°, (b) magnified XRD patterns at 2θ = 10–60°, (c) FT-IR spectra in the range of 4000–400 cm^{-1} , and (d) magnified FT-IR spectra at 1800–800 cm^{-1} for the pure SN and SN_BM powders.

surfaces of the pure SN and SN_BM10h particles were directly observed using high-resolution TEM (HR-TEM) (Fig. 4). Disordered amorphous SiO_2 was observed on the particle surfaces of both powders. The pure SN exhibited a thin SiO_2 layer of 0.6–0.8 nm (Fig. 4(a)), whereas SN_BM10h showed a thicker SiO_2 layer of 1.8–2.0 nm (Fig. 4(b)), which closely matched the value estimated from the XPS and d_{XPS} calculation results. In addition, for the SiO_2 layer in SN_BM10h, its selected area fast Fourier transform (FFT) pattern revealed its amorphous state, exhibiting a typical hollow pattern of amorphous materials (Fig. S2(a)–(c)). To further investigate the amorphous SiO_2 layer, a TEM-EDX line analysis was conducted (Fig. S3(a)–(c)). In the EDX line analysis across the SiO_2 layer, both O and N signals were detected in the amorphous SiO_2 layer region, and the O peak intensity was higher than that of N (Fig. S3(b)). Considering this together with the XPS results, it was confirmed that the amorphous layer mainly consisted of Si-O bonds derived from the surface oxidation of Si_3N_4. In addition, the peak variation behavior of N was similar to that of Si in the line profile (Figs. S3(b) and (c)); therefore, it was attributed to the interfacial N originating from the Si_3N_4 particles rather than being incorporated within the amorphous layer itself. This suggests that oxygen diffused into the surface region of Si_3N_4 particles during the mechanochemical reaction, forming O-Si-N bonds at the interface between the amorphous SiO_2 layer and the Si_3N_4 particles. This observation was consistent with the following mechanism [26]. During planetary ball milling with ultrapure water, the Si_3N_4 surface could become defective, promoting the inward diffusion of oxidizing species ($H_2O/O_2/OH^-$) and interfacial hydrolysis/oxidation, which formed an oxynitride (O-Si-N) interfacial layer and Si-OH groups. Subsequently, the continued condensation of the Si-OH groups produced an outer Si-O-Si layer. With longer milling times, the Si-O-Si layer grew thicker; thus, the surface layer was mainly composed of amorphous silica. Overall, the oxygen content increased toward the outer surface of Si_3N_4, indicating that the composition gradually transitioned to Si-O dominance.

These results suggest that planetary ball milling with ultrapure water (mechanochemical reaction) is a suitable method for SiO_2 formation on the surfaces of on Si_3N_4 particle surfaces. This surface modification was expected to facilitate improved densification during the subsequent CSP.

3.2. *Densification of pure and ball-milled Si_3N_4 powders via CSP*

To confirm the effect of the SiO_2 formation on the densification of Si_3N_4 powders via the CSP, the microstructures and relative densities of the cold-sintered pure SN and SN_BM samples were compared (Fig. 5). As shown in Fig. 5(a), the cold-sintered pure SN sample consisted of isolated particles without interparticle connections, exhibiting a morphology similar to that of the initial powder. However, under the same CSP conditions, the cold-sintered SN_BM samples exhibited significantly denser microstructures (Fig. 5(b)–(e)). In particular, with increasing milling time, interparticle connections became more evident on the fracture surfaces compared with those of the cold-sintered pure SN sample. This microstructural densification with increasing milling time was also consistent with the relative density results (Fig. 5(f)). After

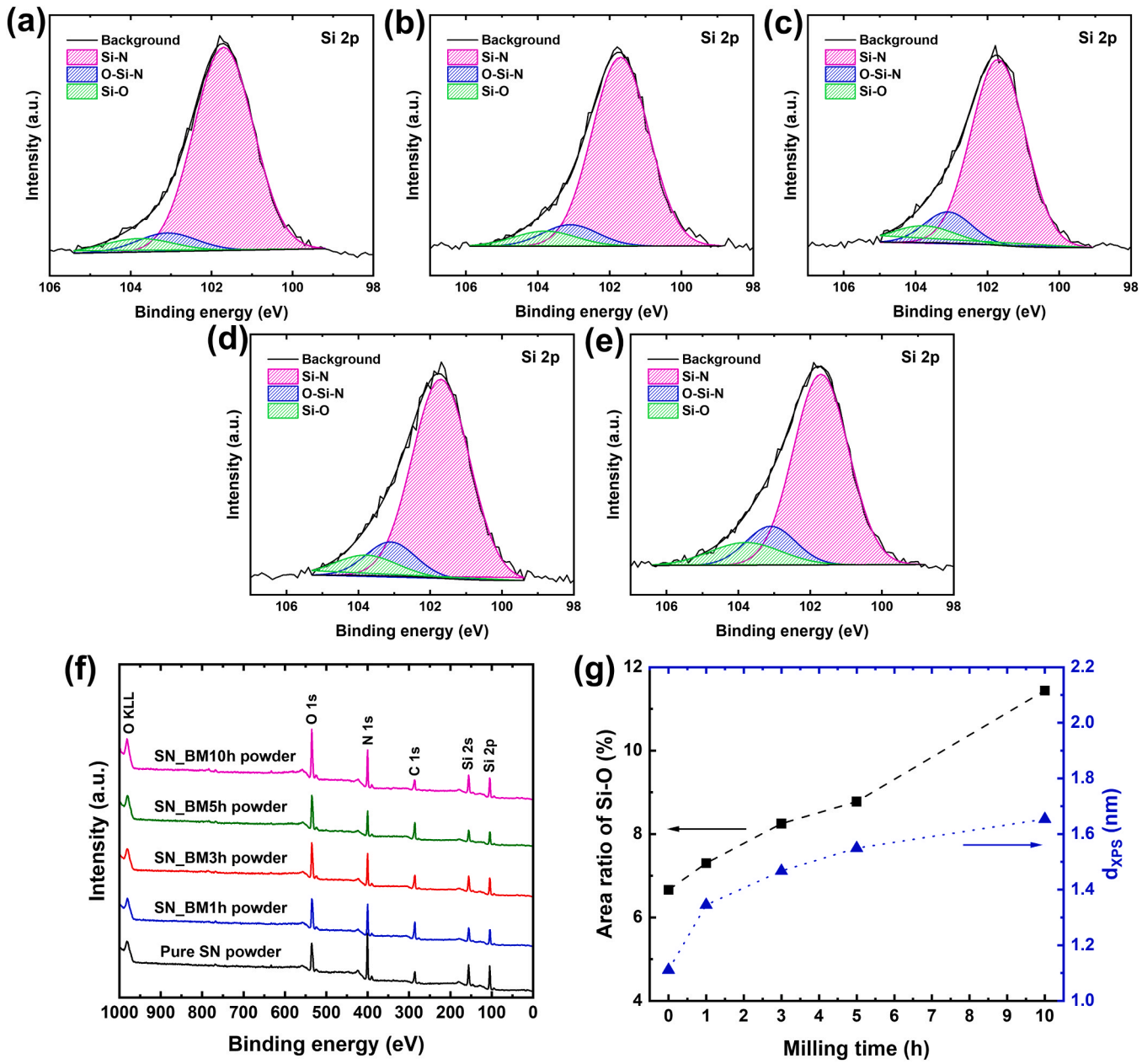

Fig. 3. XPS Si 2p spectra of the (a) pure SN, (b) SN_BM1h, (c) SN_BM3h, (d) SN_BM5h, and (e) SN_BM10h. (f) Wide-scan XPS profiles of these samples. (g) Si-O peak ratio and d_{XPS} values of the pure SN and SN_BM powders as a function of the milling time.

the CSP, the pure SN powder was densified to 62.8 % of the theoretical density. In contrast, the relative density of the cold-sintered SN_BM1h sample increased to 69.8 %. Furthermore, increasing the milling time enhanced the densification, with the SN_BM10h sample reaching a maximum relative density of 78.4 %. This improvement in the densification could be attributed to the increased formation of SiO_2. Notably, the trend for d_{XPS} to increase with the milling time (Fig. 3(g)) closely corresponded to the trend for the relative density (Fig. 5(f)), which provides strong evidence that the formation of surface SiO_2 plays a significant role in the densification of Si_3N_4 during the CSP. In addition, although the W contamination increased with the milling time, the relative density also increased. This suggests that such a small amount of contamination has little influence on the densification behavior under the present CSP conditions.

Considering the possible densification mechanism based on these results, it is assumed that SiO_2, rather than Si_3N_4, predominantly underwent dissolution–reprecipitation reactions under the CSP conditions. Several studies have reported the successful densification of various silicate-based materials via the CSP. Most of these studies employed NaOH solutions, which are highly effective in dissolving silicate materials, to promote the depolymerization and condensation reactions of the silicate networks, as shown in Eqs. (3) and (4), respectively [35–37].

$$\equiv Si-O-Si\equiv + NaOH \rightarrow \equiv Si-O-Na^{+} + \equiv Si-OH \quad (3)$$

$$\equiv Si-OH + \equiv Si-OH \rightarrow \equiv Si-O-Si\equiv + H_2O\uparrow \quad (4)$$

Furthermore, the silicate materials remained amorphous even after the CSP, despite the incorporation of Na^{+} into the silicate networks. Thus, it can be inferred that the surface amorphous SiO_2 on the Si_3N_4 particles underwent the above reactions, leading to reprecipitation, which effectively bridged the Si_3N_4 particles during densification.

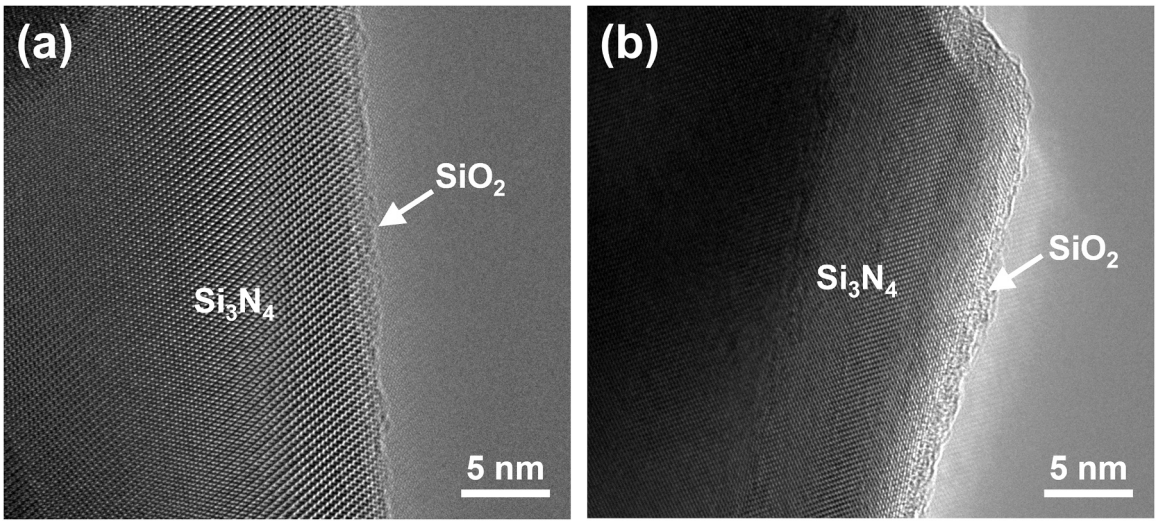

Fig. 4. HR-TEM images of the (a) pure SN and (b) SN_BM10h.

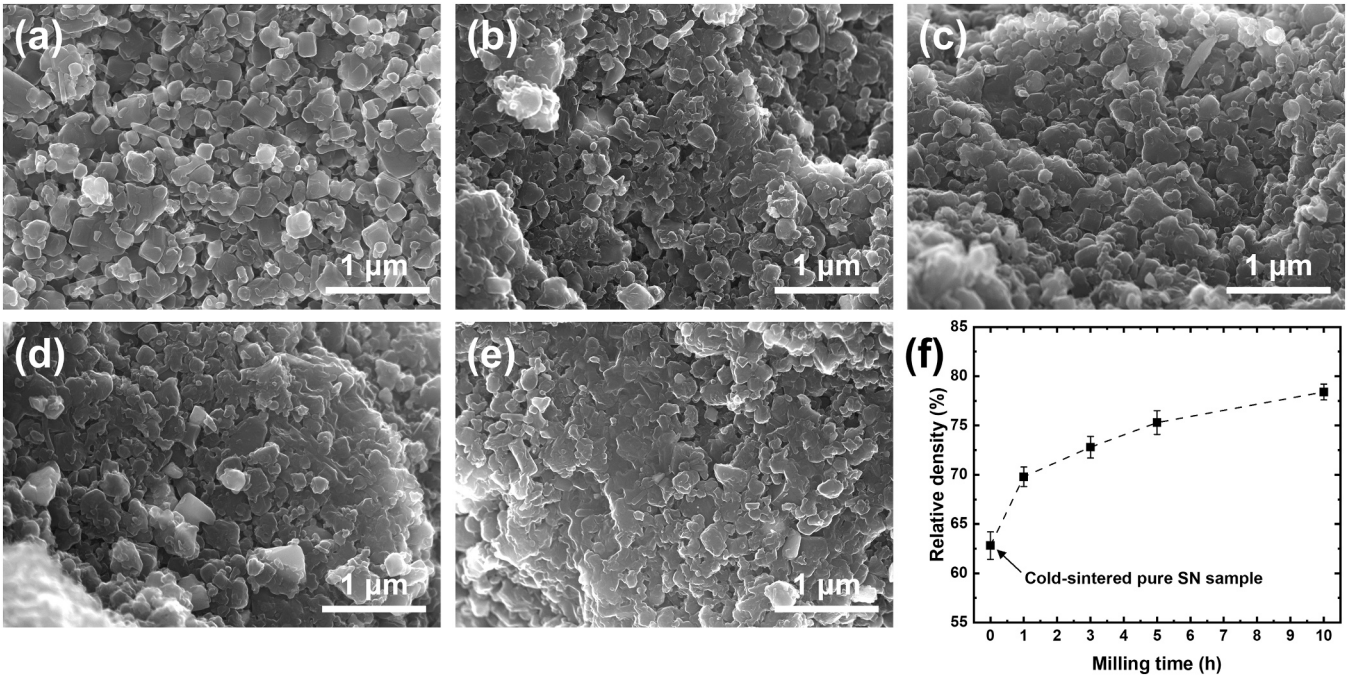

Fig. 5. Fracture surfaces of the cold-sintered samples prepared using the (a) pure SN, (b) SN_BM1h, (c) SN_BM3h, (d) SN_BM5h, and (e) SN_BM10h. (f) Relative densities of the cold-sintered pure SN and SN_BM samples plotted as a function of the milling time.

3.3. Enhanced densification through the addition of SiO_2 nanoparticles

Although the Si_3N_4 powders were densified by the CSP through the formation of amorphous SiO_2 during the mechanochemical reaction in the planetary milling step, further densification was required. The presence of numerous pores and voids in the cold-sintered SN_BM10h sample suggested that additional bonding phases may be necessary to enhance the densification of Si_3N_4. However, achieving a greater amount of amorphous SiO_2 during the milling step requires harsher conditions than those already applied, which may further increase the risk of contamination from the milling jar and balls, owing to the extremely high energy input. Therefore, to address this issue, 5 wt% amorphous SiO_2 nanoparticles were added to the Si_3N_4 powder prior to planetary milling, with the aim of enhancing the SiO_2 formation on the surfaces of the Si_3N_4 particles during milling. After milling, the amount of SiO_2 formed in the SN/5SiO_2_BM powder was evaluated as a function of the milling time using TEM and XPS (Figs. 6 and 7, respectively). As shown in Fig. 6, the added SiO_2 nanoparticles were observed between the Si_3N_4 particles, regardless of the milling time. In particular, compared with the SN_BM10h powder (Figs. S2(a) and (b)), the SN/5SiO_2_BM10h powder clearly exhibited SiO_2 nanoparticles uniformly dispersed within the interparticle regions of the Si_3N_4 particles (Figs. S2 (d) and (e)). Despite the presence of residual SiO_2 nanoparticles, an increase in milling time led to the formation of more SiO_2 on the surfaces of the Si_3N_4 particles, resulting in a thicker SiO_2 layer (inset HR-TEM images in Fig. 6), which was consistent with the results presented in the previous section. Interestingly, compared to the SN_BM10h sample, the SN/5SiO_2_BM10h sample exhibited an almost three-fold thicker SiO_2 layer (approximately 6 nm) on its surface under the same milling time, as shown in the inset HR-TEM image in Fig. 6(d). This suggests that the

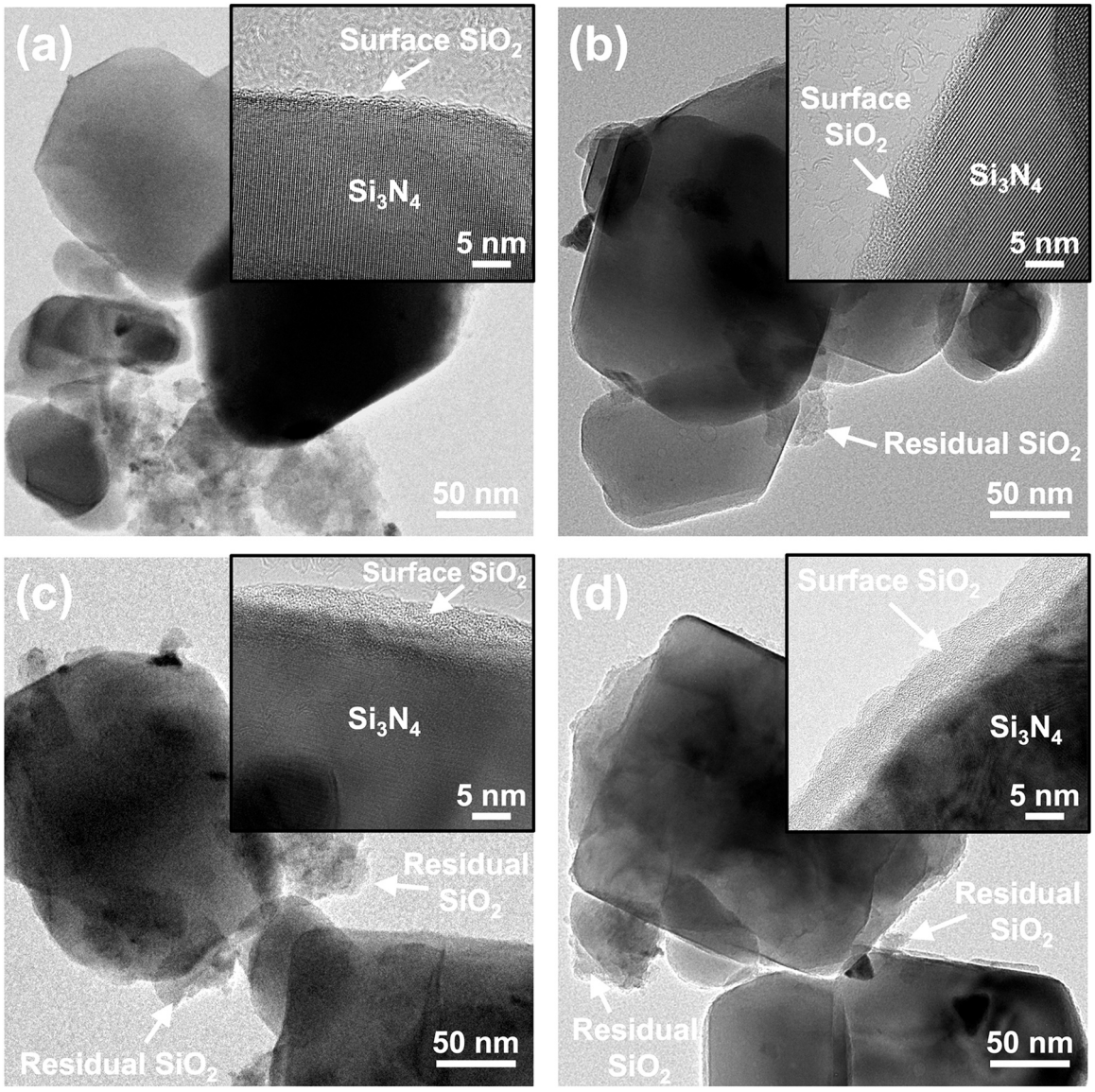

Fig. 6. TEM images of (a) SN/5SiO_2_BM1h, (b) SN/5SiO_2_BM3h, (c) SN/5SiO_2_BM5h, and (d) SN/5SiO_2_BM10h, with the insets showing HR-TEM images at a higher magnification.

added SiO_2 nanoparticles served as additional precursors for the formation of SiO_2 on the surfaces during the milling step via a mechanochemical reaction. In addition, this surface SiO_2 layer was observed to be disordered amorphous SiO_2 (Fig. S2(f)), while the residual nanoparticles remained amorphous (Fig. S2(g) and (h)), exhibiting typical hollow FFT patterns. Furthermore, as shown in Fig. S3(d)–(f), SN/5SiO_2_BM10h also exhibited a TEM-EDX line analysis result similar to that of SN_BM10h, where the O peak was more intense than N, suggesting that the amorphous layer was mainly silica-rich with minor O-Si-N bonding near the Si_3N_4 interface.

Fig. 7 presents XPS analysis results for the SN/5SiO_2_BM samples. The spectrum was deconvoluted into three peaks, and the Si-O peak area ratio was calculated using the method described above. The d_{XPS} calculation method (Eq. (1)) assumed that all of the SiO_2 was present as a uniform surface layer. However, in these samples, the added SiO_2 nanoparticles not only facilitated the formation of a SiO_2 surface layer, but also remained distributed within the interparticle regions of the Si_3N_4 particles. Therefore, the d_{XPS} values were not calculated for these samples. Consistent with the previous results, an increase in the milling time led to a gradual increase in the area of the Si-O peak (Fig. 7(a)–(d)). As shown in Fig. 7(e), for the SN/5SiO_2_BM1h sample, the Si-O peak area ratio was determined to be 13.7 %, which was higher than that of SN_BM10h (11.4 %). Additionally, the Si-O peak area ratio further increased with the milling time, reaching 25.8 % after 10 h of planetary ball milling (SN/5SiO_2_BM10h). For the SN_BM samples, the Si-O peak area ratio increased from 7.2 % to 11.4 % when the planetary ball milling was increased from 1 h to 10 h (Fig. 3(g)). In contrast, the SN/5SiO_2_BM sample exhibited a 12.1 % increase over the same milling period. Although the absolute peak area was naturally larger owing to the addition of 5 wt% SiO_2 nanoparticles, the considerable increase during the same period further supported the idea that the addition of SiO_2 nanoparticles promoted the formation of a SiO_2 layer on the surfaces of the Si_3N_4 particles through the mechanochemical reaction.

The SN/5SiO_2_BM powder was densified under the same CSP conditions (Fig. 8). As shown in Fig. 8(a), the relative density increased with the milling time. The cold-sintered SN/5SiO_2_BM1h sample exhibited a relative density of 72.0 %, which was higher than that of the cold-sintered SN_BM1h sample, and after milling for 10 h, the relative density increased to 86.2 %, which was approximately 10 % higher than that of the cold-sintered SN_BM10h sample. These values were

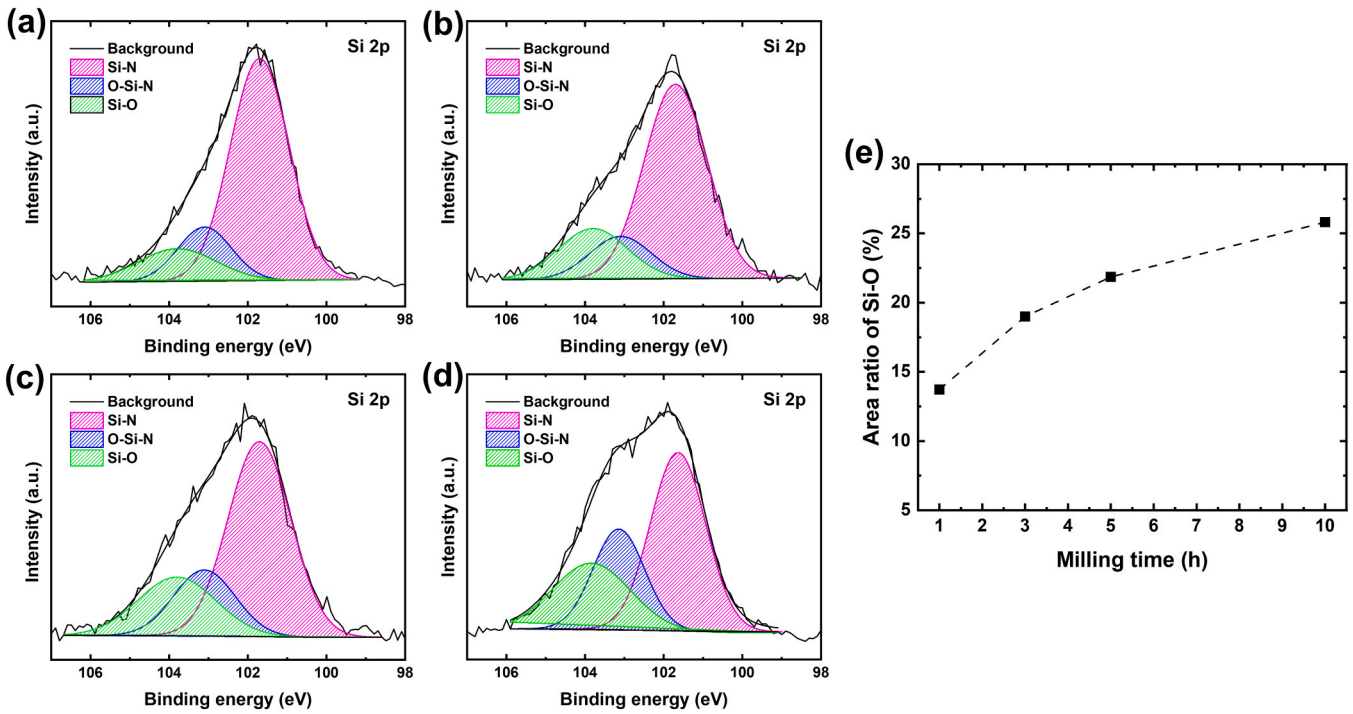

Fig. 7. XPS Si 2p spectra of (a) SN/5SiO_2_BM1h, (b) SN/5SiO_2_BM3h, (c) SN/5SiO_2_BM5h, and (d) SN/5SiO_2_BM10h. (e) Si-O peak ratio of SN/5SiO_2_BM powders as a function of the milling time.

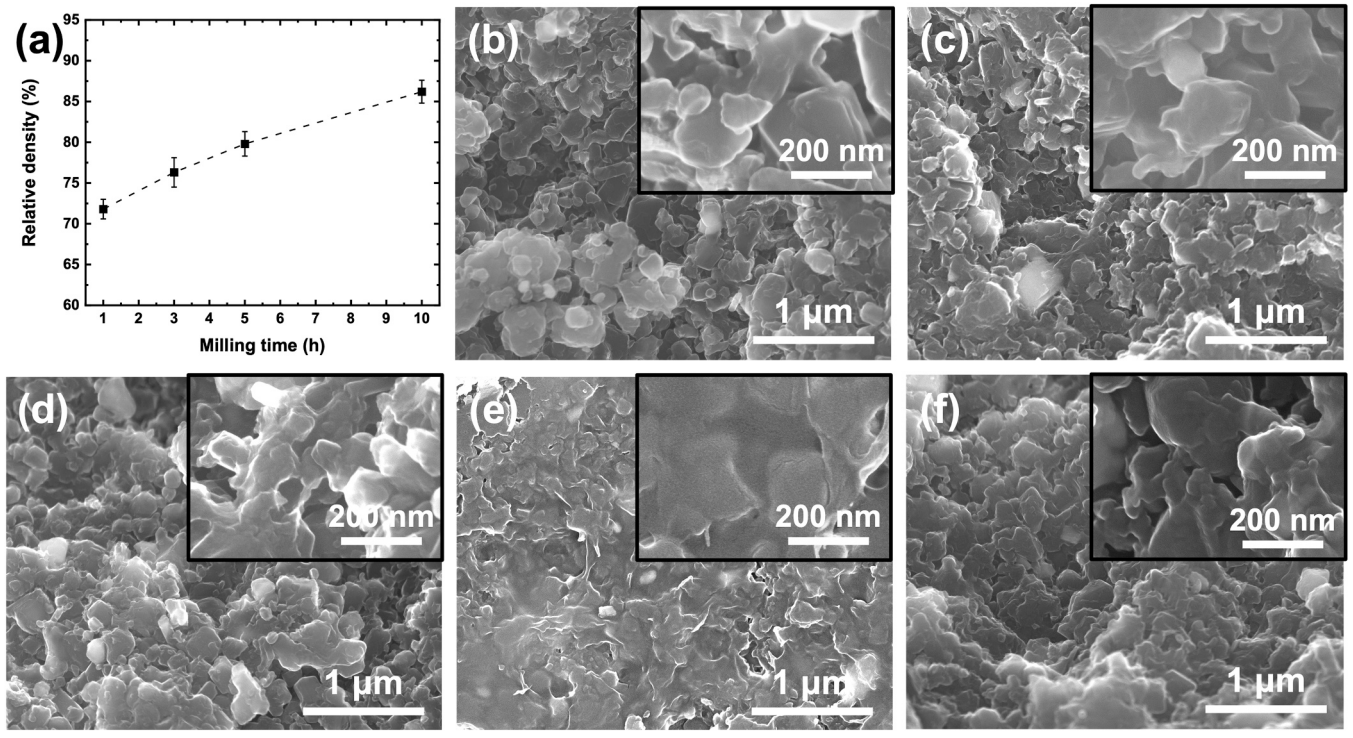

Fig. 8. (a) Relative densities of the cold-sintered SN/5SiO_2_BM samples. Fracture surface images of the cold-sintered (b) SN/5SiO_2_BM1h, (c) SN/5SiO_2_BM3h, (d) SN/5SiO_2_BM5h, and (e) SN/5SiO_2_BM10h samples, along with that of (f) a sample obtained by simply mixing SN_BM10h powder with 5 wt% SiO_2 nanoparticles.

significantly higher than those of the cold-sintered pure SN and SN_BM samples. Thus, the addition of 5 wt% SiO_2 nanoparticles accelerated the dissolution–reprecipitation mechanism of amorphous SiO_2, which increased the densification of the Si_3N_4 particles during the CSP. Furthermore, the relative density achieved in this study was higher than those reported in previous cold-sintering studies on Si_3N_4[21,22]. As shown in Fig. 8(b)–(e), the fracture surfaces of the cold-sintered SN/5SiO_2_BM samples exhibited a denser microstructure than those of the cold-sintered pure SN and SN_BM samples. Although some pores remained across the entire fracture surface, the cold-sintered SN/5SiO_2_BM10h sample exhibited a partially highly densified region (highlighted in the high-magnification image in Fig. 8(e)), indicating a

particle-to-particle connection with almost no vacant spaces. To further investigate the effect of adding 5 wt% SiO_2 during planetary ball milling, the SN_BM10h powder was mixed with 5 wt% SiO_2 nanoparticles and cold-sintered under the same conditions. This simply mixed powder achieved a relative density of 80.6 %, which was approximately 6 % lower than that of the cold-sintered SN/5SiO_2_BM10h sample, despite using the same milling time. In addition, compared with the fracture surface of the cold-sintered SN/5SiO_2_BM10h, the cold-sintered simply mixed powder exhibited more pores and vacant areas (Fig. 8(f)). These findings suggest that incorporating SiO_2 nanoparticles during the milling process is more effective in enhancing densification, likely because of the surface SiO_2 phases and their uniform distribution among the particles.

To investigate the Si_3N_4/SiO_2 interfaces, the cross-sectional microstructure of the cold-sintered SN/5SiO_2_BM10h sample was examined using HR-TEM (Fig. 9(a)). The results confirmed that the spaces between the Si_3N_4 particles were filled with the SiO_2 phase, which acted as a bonding phase and contributed to the densification. As shown in Fig. 9 (b), this SiO_2 phase exhibited a disordered amorphous state, indicating that the amorphous SiO_2 layer on the Si_3N_4 surface remained as an amorphous bonding phase even after the CSP. Furthermore, the results inferred that both the surface SiO_2 and residual SiO_2 nanoparticles participated in depolymerization–condensation during the CSP, resulting in the formation of a bonding phase between the Si_3N_4 particles. Overall, this microstructural feature resembled the grain and grain boundary phases of Si_3N_4 ceramics, which are typically observed during liquid-phase sintering at high temperatures. Thus, the effective use of the amorphous SiO_2 bonding phase enabled the achievement of a relative density of 86.2 % at a significantly low temperature of 160 °C. Furthermore, this demonstrated the application of the CSP densification mechanism to Si_3N_4 particles, which are typically challenging for solvents to break down.

3.4. Phase analysis and mechanical properties of cold-sintered SN/5SiO_2_BM samples

The phase structures of the cold-sintered SN/5SiO_2_BM samples were analyzed using XRD (Fig. 10(a)). All of the cold-sintered samples exhibited crystalline peaks corresponding to α-Si_3N_4 (PDF no. 00–041–0360), indicating that the phase consisted entirely of the α phase as a result of the low sintering temperature (160 °C).

To investigate the densification behavior and associated mechanical properties, the Vickers hardness, biaxial flexural strength, and Young's modulus of the cold-sintered SN/5SiO_2_BM samples were measured and plotted with respect to the milling time (Fig. 10(b)–(d)). All of the mechanical properties improved almost linearly with increasing milling time. In particular, the Vickers hardness increased from 1.47 ± 0.07–2.53 ± 0.09 GPa as the milling time increased from 1 to 10 h. In addition to the Vickers hardness, the biaxial flexural strength increased from 91.2 ± 13.8–169.4 ± 12.3 MPa, while the Young's modulus increased from 57.3 ± 2.2–113.1 ± 1.5 GPa over the same period. Because almost no changes in the crystal structure were observed in the XRD patterns (Fig. 10(a)), the increase was attributed to enhanced densification resulting from the increased formation of amorphous SiO_2 layers on the Si_3N_4 particle surfaces with increasing milling time. Although these values did not reach those typically attained by conventional high-temperature sintering methods [11–15,38,39], the Vickers hardness observed in the present work was significantly higher than those of previously reported cold-sintered Si_3N_4-based composites [21], likely owing to the improved densification achieved in this study. These results suggest that the mechanochemical approach is an effective strategy for generating a SiO_2 bonding phase, thereby facilitating the densification of otherwise insoluble materials such as Si_3N_4 via the CSP. Additionally, the enhanced microstructural connectivity and mechanical strength achieved at the remarkably low sintering temperature of 160 °C demonstrated the feasibility of this energy-efficient densification method and highlighted its potential for future applications.

4. Conclusions

To densify Si_3N_4 powder using the CSP, an amorphous SiO_2 layer was effectively introduced onto the surface of the Si_3N_4 particles through a mechanochemical reaction induced by planetary ball milling at room temperature with ultrapure water. The incorporated amorphous SiO_2 acted as a bonding phase, enabling the densification of Si_3N_4 to a maximum relative density of 78.4 % at a significantly lower temperature of 160 °C. Furthermore, the addition of 5 wt% SiO_2 nanoparticles prior to the planetary ball milling of the Si_3N_4 powder enhanced the densification by promoting the formation of a bonding phase to connect the Si_3N_4 particles, achieving the highest relative density of 86.2 % at the same temperature. With an increase in the milling time, denser microstructures with fewer pores were observed on the fractured surfaces. The mechanical properties also improved with increases in the milling time and densification, reaching maximum values of 2.53 ± 0.09 GPa for the Vickers hardness, 169.4 ± 12.3 MPa for the biaxial flexural strength, and 113.1 ± 1.5 GPa for Young's modulus. These results demonstrated a novel low-temperature sintering strategy for densifying solution-insoluble Si_3N_4 powders by utilizing a mechanochemical reaction to form a soluble bonding phase in the CSP, suggesting its potential applicability to other solution-insoluble ceramic systems.

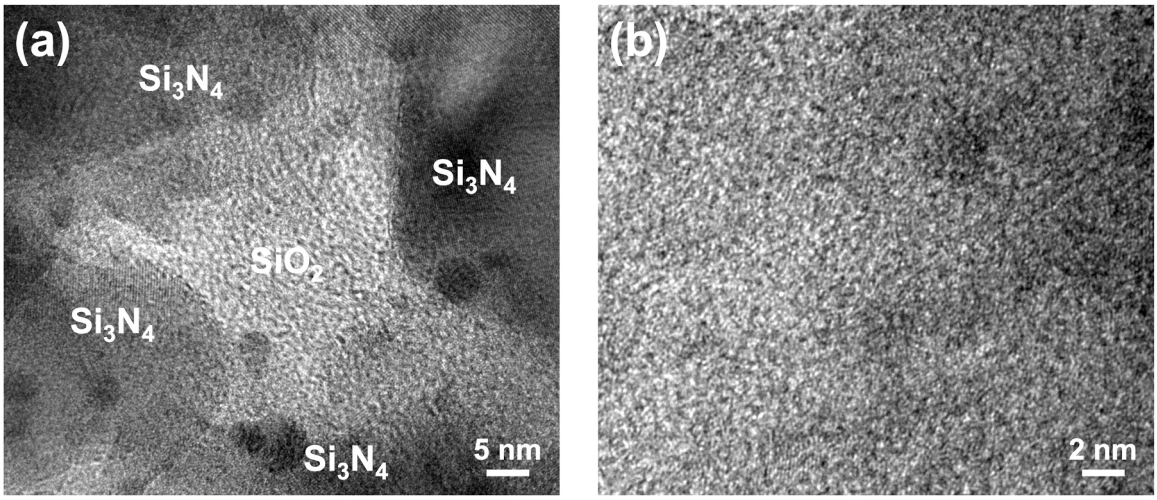

Fig. 9. HR-TEM image of (a) the cold-sintered SN/5SiO_2_BM10h sample and (b) a high-magnification view of the amorphous SiO_2 bonding phase.

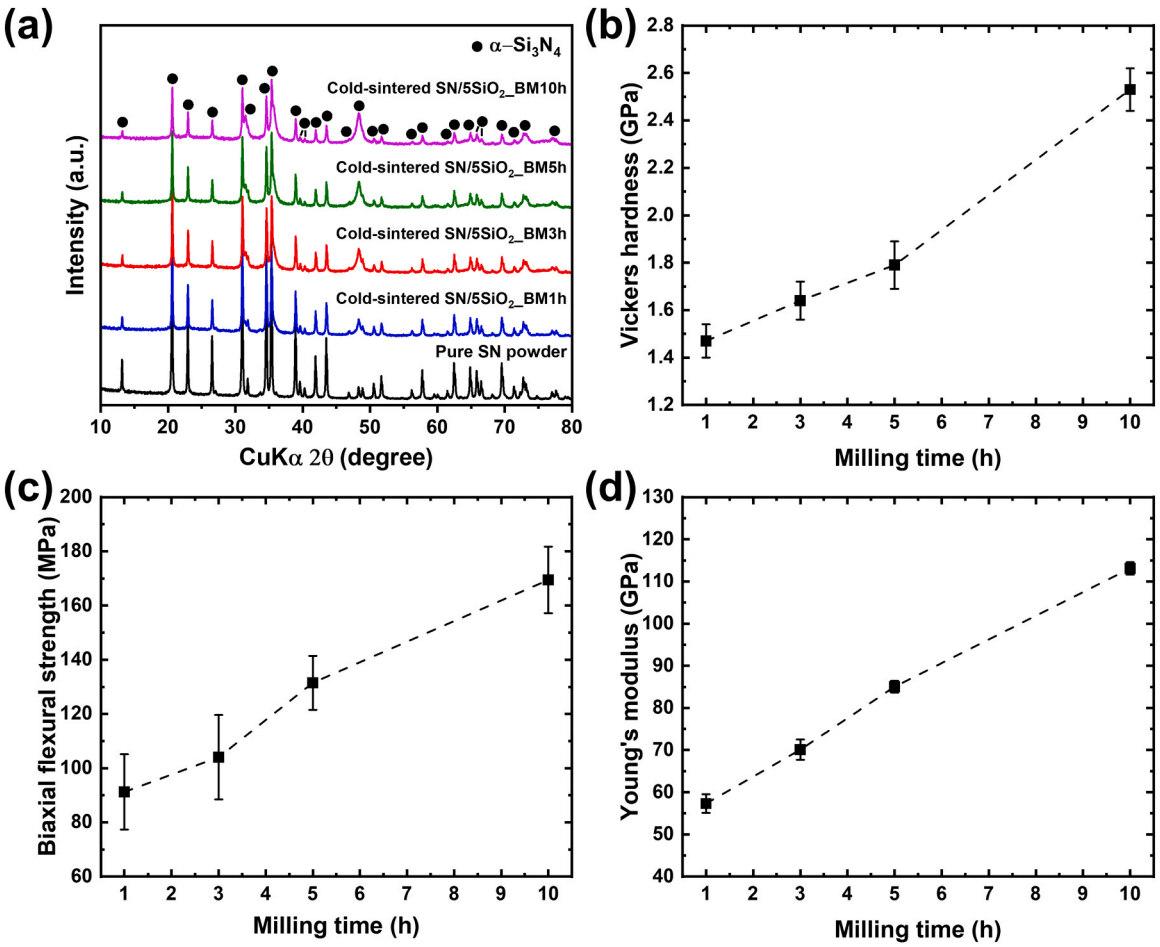

Fig. 10. (a) XRD patterns, (b) Vickers hardness, (c) biaxial flexural strength, and (d) Young's modulus of the cold-sintered SN/5SiO_2_BM samples.

CRediT authorship contribution statement

Tomoyo Goto: Writing – review & editing, Methodology, Investigation. **Yoshifumi Kondo:** Writing – review & editing, Methodology, Investigation. **Masaya Minehira:** Writing – review & editing, Methodology, Investigation, Formal analysis. **Sunghun Cho:** Writing – review & editing, Methodology, Investigation, Formal analysis. **Do Hyung Han:** Writing – review & editing, Investigation, Formal analysis. **Tohru Sekino:** Writing – review & editing, Supervision, Methodology, Funding acquisition, Conceptualization. **Yeongjun Seo:** Writing – review & editing, Writing – original draft, Supervision, Methodology, Investigation, Funding acquisition, Formal analysis, Conceptualization.

Declaration of Competing interest

The authors declare that they have no known competing financial interests or personal relationships that could have appeared to influence the work reported in this paper.

Acknowledgement

This work was supported by the program "Dynamic Alliance for Open Innovation Bridging Human, Environment and Materials" in "Network Joint Research Center for Materials and Devices" (MEXT, Japan) and JSPS Grant-in-Aid for Early-Career Scientists [grant number JP22K14476]. The XPS and TEM observations were performed at the Comprehensive Analysis Center, SANKEN, The University of Osaka, Japan. The authors are grateful to Mr. Y. Murakami (The University of Osaka, Japan) for his technical support in TEM observations. This work was the result of using research equipment shared in MEXT Project for Promoting Public Utilization of Advanced Research Infrastructure (Program for Supporting Construction of Core Facilities) [grant number JPMXS0441200024].

Appendix A. Supporting information

Supplementary data associated with this article can be found in the online version at doi:10.1016/j.jallcom.2025.184716.

References

[1] C.C. Ye, H.Q. Ru, D.L. Chen, Fatigue behavior of silicon nitride ceramics, Ceram. Int. 49 (2023) 28405–28414, https://doi.org/10.1016/j.ceramint.2023.06.095.
[2] X. Dong, J. Wu, H. Yu, Q. Zhou, W. Wang, X. Zhang, L. Zhang, L. Li, R. He, Additive manufacturing of silicon nitride ceramics: a review of advances and perspectives, Int. J. Appl. Ceram. Technol. 19 (2022) 2929–2949, https://doi.org/10.1111/ijac.14162.
[3] L. Wang, L. Wang, Z. Hao, W. Tang, R. Dou, Microstructure and properties of silicon nitride ceramics fabricated by vat photopolymerization in combination with pressureless sintering, Ceram. Int. 50 (2024) 10485–10496, https://doi.org/10.1016/j.ceramint.2023.12.361.
[4] S. Du, J. Zhang, F. Li, Z. Chen, S. Zhang, S. Zhao, W. Cui, K. Chen, G. Liu, Effect of initial phase composition on the phase composition, microstructure, and mechanical properties of Si_3N_4 ceramics, J. Am. Ceram. Soc. 107 (2024) 2556–2564, https://doi.org/10.1111/jace.19584.
[5] T. Cheng, J. Lv, D. Wu, D. Wu, Effects of microstructures on the fracture properties of silicon nitride ceramics at elevated temperatures, Int. J. Appl. Ceram. Technol. 22 (2025) e14942, https://doi.org/10.1111/ijac.14942.
[6] D. Wen, S. Wang, G. Wang, P. Guo, L. Yang, X. Yang, Fabrication processing and mechanical properties of Si_3N_4 ceramic turbocharger wheel, Ceram. Int. 44 (2018) 10596–10603, https://doi.org/10.1016/j.ceramint.2018.03.084.
[7] N.K. Georgiu, E.S. Zhukova, A.I. Zhmurin, A.I. Ganichev, M.G. Lisachenko, M. Yu Rusin, Mechanical properties of silicon nitride ceramics containing Yb_2O_3

sintering additives, Inorg. Mater. 60 (2024) 1505–1513, https://doi.org/10.1134/S0020168525700207.
[8] C. Wei, S. Li, Y. Wang, Research on the friction and wear mechanism of Si_3N_4 bearing materials under low temperature conditions, J. Mater. Eng. Perform. 34 (2025) 18697–18711, https://doi.org/10.1007/s11665-024-10559-7.
[9] C. Luo, N. Li, T. Deng, Enhancement of Si3N4 ceramics via evolution of grain interface between ZrO2 and Si3N4 under pressureless sintering, J. Am. Ceram. Soc. 106 (2023) 7043–7056, https://doi.org/10.1111/jace.19263.
[10] K. Kumar, M.-J. Kim, H.-M. Oh, Y.-J. Park, H.-N. Kim, H.J. Ma, J.-W. Lee, J.-W. Ko, Fabrication of highly dense Si_3N_4 via record low-content additive system for low-temperature pressureless sintering, J. Am. Ceram. Soc. 105 (2022) 4669–4680, https://doi.org/10.1111/jace.18467.
[11] B. Ma, Y. Tang, C. Deng, Effects of Al_2O_3–Y_2O_3/Yb_2O_3 additives on microstructures and mechanical properties of silicon nitride ceramics prepared by hot-pressing sintering, Int. J. Appl. Ceram. Technol. 19 (2022) 2523–2532, https://doi.org/10.1111/ijac.14081.
[12] Y. Zhao, Y. Zhang, H. Gong, H. Sun, Q. Li, Gas pressure sintering of BN/Si_3N_4 wave-transparent material with Y_2O_3-MgO nanopowders addition, Ceram. Int. 40 (2014) 13537–13541, https://doi.org/10.1016/j.ceramint.2014.05.054.
[13] J. Tatami, D. Hiratsuka, S. Okada, K. Komeya, T. Wakihara, Analysis of sintering behavior of silicon nitride based on master sintering curve theory of liquid phase sintering, J. Ceram. Soc. Jpn. 124 (2016) 375–380, https://doi.org/10.2109/jcersj2.15291.
[14] P. Uyan, Ö. Cengiz, S. Turan, An investigation on the thermal and microstructural properties of low-cost pressureless sintered silicon nitride (Si_3N_4) ceramics incorporated with Y_2O_3-SiO_2-MgO, J. Aust. Ceram. Soc. 58 (2022) 1433–1443, https://doi.org/10.1007/s41779-022-00779-2.
[15] Y. Li, H.-N. Kim, H. Wu, M.-J. Kim, J.-W. Ko, Y.-J. Park, Z. Huang, H.-D. Kim, Microstructure and thermal conductivity of gas-pressure-sintered Si_3N_4 ceramic: the effects of Y_2O_3 additive content, J. Eur. Ceram. Soc. 41 (2021) 274–283, https://doi.org/10.1016/j.jeurceramsoc.2020.08.035.
[16] H. Guo, A. Baker, J. Guo, C.A. Randall, Cold sintering process: a novel technique for low-temperature ceramic processing of ferroelectrics, J. Am. Ceram. Soc. 99 (2016) 3489–3507, https://doi.org/10.1111/jace.14554.
[17] A. Galotta, V.M. Sglavo, The cold sintering process: A review on processing features, densification mechanisms and perspectives, J. Eur. Ceram. Soc. 41 (2021) 1–17, https://doi.org/10.1016/j.jeurceramsoc.2021.09.024.
[18] H. Guo, A. Baker, J. Guo, C.A. Randall, Protocol for ultralow-temperature ceramic sintering: an integration of nanotechnology and the cold sintering process, ACS Nano 10 (2016) 10606–10614, https://doi.org/10.1021/acsnano.6b03800.
[19] K. Yamaguchi, G. Lee, S. Hashimoto, Cold sintering of SiC ceramics with the assistance of amorphous SiO_2 surface layer, Ceram. Int. 48 (2022) 37362–37369, https://doi.org/10.1016/j.ceramint.2022.08.313.
[20] I.J. Induja, M.T. Sebastian, Microwave dielectric properties of cold sintered Al_2O_3-NaCl composite, Mater. Lett. 211 (2018) 55–57, https://doi.org/10.1016/j.matlet.2017.09.083.
[21] D. Gu, G. Wang, X. Chen, Z. Liu, S. Chen, H. Xie, SiO_2 shell thickness affects the tribological properties of Si_3N_4@SiO_2/PEEK core–shell composite prepared by cold sintering, Mater. Lett. 345 (2023) 134488, https://doi.org/10.1016/j.matlet.2023.134488.
[22] D. Gu, G. Wang, S. Chen, H. Luo, X. Chen, Z. Liu, Si_3N_4@SiO_2/PEEK core-shell structure ceramic matrix composite prepared by cold sintering and its tribological properties, Ceram. Int. 50 (2024) 15896–15904, https://doi.org/10.1016/j.ceramint.2024.02.070.
[23] Y. Shi, Z. Huang, Y. Lin, B. Wang, Y. Xie, Q. Zhou, J. Yao, C. Zhang, X. Chen, L. Liu, J. Pan, In situ formation of carbon-based tribo-films via engineered composite design for enhanced anti-adhesion performance in metallic contacts, Wear 580581 (2025) 206271, https://doi.org/10.1016/j.wear.2025.206271.
[24] Z. Jiao, Y. Dong, Q. Li, Q. Zhou, S. Han, C. Yin, Z. Huang, X. Wang, H. Wang, W. Liu, Enhancing tribocorrosion resistance of VCoNi alloys in artificial seawater via nitrogen alloying, Corros. Sci. 243 (2025) 112600, https://doi.org/10.1016/j.corsci.2024.112600.
[25] S.J. Hong, S. Nam, Simple synthesis of SiO_x by high-energy ball milling as a promising anode material for Li-ion batteries, Corros. Sci. Technol. 21 (2022) 445–453, https://doi.org/10.14773/CST.2022.21.6.445.
[26] G. Pezzotti, Silicon nitride as a biomaterial, J. Ceram. Soc. Jpn. 131 (2023) 398–428, https://doi.org/10.2109/jcersj2.23057.
[27] X. Du, S.S. Lee, G. Blugan, S.J. Ferguson, Silicon nitride as a biomedical Material: An overview, Int. J. Mol. Sci. 23 (2022), https://doi.org/10.3390/ijms23126551.
[28] L. Shuangyu, P. Mingbo, L. Ping, L. Cong, W. Binhua, Z. Fulong, T.M. Vasilieva, H. Chuanjin, W. Xi, H. Juan, Surface modification of Si_3N_4 via silane coating and oxidation for photocurable slurry preparation, Ceram. Int. 51 (2025) 5381–5396, https://doi.org/10.1016/j.ceramint.2024.11.511.
[29] J. Haines, C. Levelut, A. Isambert, P. Hébert, S. Kohara, D.A. Keen, T. Hammouda, D. Andrault, Topologically ordered amorphous silica obtained from the collapsed siliceous zeolite, silicalite-1-F: a step toward “perfect” glasses, J. Am. Chem. Soc. 131 (2009) 12333–12338, https://doi.org/10.1021/ja904054v.
[30] S. Islam, R.A. Rahman, Z. Othaman, S. Riaz, M.A. Saeed, S. Naseem, Preparation and characterization of crack-free sol-gel based SiO_2-TiO_2 hybrid nanoparticle film, J. Sol. Gel Sci. Technol. 68 (2013) 162–168, https://doi.org/10.1007/s10971-013-3147-x.
[31] Z. Ni, J. Jiang, X. Yang, X. Yang, Z. Zhou, Q. He, Surface characterization of silicon nitride powder and electrokinetic behavior of its aqueous suspension, Ceram. Int. 46 (2020) 9530–9537, https://doi.org/10.1016/j.ceramint.2019.12.215.
[32] S.M. Castanho, R. Moreno, J.L.G. Fierro, Influence of process conditions on the surface oxidation of silicon nitride green compacts, J. Mater. Sci. 32 (1997) 157–162, https://doi.org/10.1023/A:1018543703475.
[33] Z. Hu, J. Liu, Z. Xie, Synthesis of α-Si_3N_4 whiskers or equiaxed particles from amorphous Si_3N_4 powders, Ceram. Int. 46 (2020) 23734–23741, https://doi.org/10.1016/j.ceramint.2020.06.147.
[34] H. Cheng, N. Garcia-Araez, A.L. Hector, Enhancing the performance of hard carbon for sodium-ion batteries by coating with silicon nitride/oxycarbide nanoparticles, Mater. Adv. 2 (2021) 7956–7966, https://doi.org/10.1039/D1MA00613D.
[35] L. Karacasulu, E. Ogur, C. Piskin, C. Vakifahmetoglu, Cold sintering of soda-lime glass, Scr. Mater. 192 (2021) 111–114, https://doi.org/10.1016/j.scriptamat.2020.10.015.
[36] X. Lyu, Y. Seo, D.H. Han, S. Cho, T. Goto, T. Sekino, Roles of alkali ions in densification process of cold sintered lithium disilicate glass materials, Ceram. Int. 50 (2024) 7567–7576, https://doi.org/10.1016/j.ceramint.2023.12.068.
[37] J. Gao, K. Wang, W. Luo, X. Cheng, Y. Fan, W. Jiang, Realizing translucency in aluminosilicate glass at ultralow temperature via cold sintering process, J. Adv. Ceram. 11 (2022) 1714–1724, https://doi.org/10.1007/s40145-022-0642-y.
[38] H. Marulcuoglu, F. Kara, Microstructure and mechanical properties of dense Si_3N_4 ceramics prepared by direct coagulation casting and cold isostatic pressing, Mater. Sci. Eng. A 854 (2022) 143782, https://doi.org/10.1016/j.msea.2022.143782.
[39] P.V. Andreev, P.D. Drozhilkin, L.S. Alekseeva, K.E. Smetanina, G.V. Scherbak, A. A. Popov, M.S. Boldin, Physical and mechanical properties of ceramics based on Si_3N_4 of various dispersion with 3% Y_2O_3-Al_2O_3, Inorg. Mater. Appl. Res. 15 (2024) 470–479, https://doi.org/10.1134/S2075113324020047.